AC Colaitis et al.

Influence of laser induced hot electrons on the threshold for shock ignition of fusion reactions

Influence of laser induced hot electrons on the threshold for shock ignition of fusion reactions

A. Colaïtis,[1] X. Ribeyre,[1] E. Le Bel,[1] G. Duchateau,[1] Ph. Nicolaï,[1] and V. Tikhonchuk[1]

Université de Bordeaux - CNRS - CEA, Centre Lasers Intenses et Applications, UMR 5107,
351 Cours de la Libération, 33400 Talence, France

(Dated: 12 April 2016)

The effects of Hot Electrons (HE) generated by the nonlinear Laser-Plasma Interaction (LPI) on the dynamics of Shock Ignition Inertial Confinement Fusion targets is investigated. The coupling between the laser beam, plasma dynamics and hot electron generation and propagation is described with a radiative hydrodynamics code using an inline model based on Paraxial Complex Geometrical Optics [Colaïtis et al., Phys. Rev. E 92, 041101 (2015)]. Two targets are considered: the pure-DT HiPER target and a CH-DT design with baseline spike powers of the order of 200-300 TW. In both cases, accounting for the LPI-generated HEs leads to non-igniting targets when using the baseline spike powers. While HEs are found to increase the ignitor shock pressure, they also preheat the bulk of the imploding shell, notably causing its expansion and contamination of the hotspot with the dense shell material before the time of shock convergence. The associated increase in hotspot mass (i) increases the ignitor shock pressure required to ignite the fusion reactions and (ii) significantly increases the power losses through Bremsstrahlung X-ray radiation, thus rapidly cooling the hotspot. These effects are less prominent for the CH-DT target where the plastic ablator shields the lower energy LPI-HE spectrum. Simulations using higher laser spike powers of 500 TW suggest that the CH-DT capsule marginally ignites, with an ignition window width significantly smaller than without LPI-HEs, and with three quarters of the baseline target yield. The latter effect arises from the relation between the shock launching time and the shell areal density, which becomes relevant in presence of a LPI-HE preheating.

I. INTRODUCTION

Shock Ignition (SI) in Inertial Confinement Fusion (ICF) is an alternative ignition scheme where the compression and ignition phases are separated: the target compression is conducted at a low velocity using lasers of moderate energy and the ignition is achieved at the end of the compression phase with a dedicated intense laser pulse[1–3], so-called spike. The latter launches a strong shock in the target, thus raising the hotspot pressure and temperature above the ignition threshold when the cold shell is assembled. The attractiveness of this ignition scheme notably lies in its effective simplicity: the required pulse shapes being available on the current generation of high power laser facilities and the required targets being of the same order of complexity than direct-drive hotspot scheme targets[4]. By decoupling the compression and the heating phase, much lower laser energies are required (of the order of 500 kJ) for the obtention of similar target yields, thus making it potentially easier to implement.

In order to obtain the required temperatures for ignition in a hotspot of ~ 50 μm radius, an ignitor shock pressure of the order of 30 GBar is required. Considering the ablation pressures of the order of 150-300 MBar estimated in shock ignition experiments in planar[5–7] and spherical[7–9] geometries, the shock converging in the shell must be amplified by a factor ~ 100-200[10,11]. The amplification of the shock pressure depends on (i) spherical convergence effects and (ii) the precise timing of the shock collision with the diverging shock from the laser

pulse used for the compression[12]. Hydrodynamic estimates from simulations that do not include nonlinear Laser-Plasma Interactions (LPI) predict that the amplification factors of the order of 100-200 can be achieved, albeit in a narrow timing window and using laser intensities for the spike pulse of the order of 5×10^{15} - 10^{16} W/cm^2. While the compression phase is less sensible to HE preheat and symmetry breaking issues than the standard hotspot scheme because of a lower laser intensity, the laser spike employed for the generation of the strong shock lies in a strongly nonlinear interaction regime[13–16]. Considering typical spike durations of ~ 500 ps at peak intensity, nonlinear LPIs have ample time to develop and (i) drive copious amounts of high energy supra-thermal electrons, notably via the excitation of Electron Plasma Waves (EPW) from the Stimulated Raman Scattering (SRS) and Two-Plasmon Decay (TPD) instabilities[8,15,17,18], and (ii) significantly reduce the laser-target coupling for the strong shock generation through Crossed Beam Energy Transfer (CBET). Although the shock ignition scheme promises higher gains and better robustness to hydrodynamical instabilities than the conventional hotspot ignition scheme, the physics of the laser-plasma interaction must be carefully investigated, especially during the laser spike where new physical issues arise[16], related to the generation and amplification of strong shocks and the interaction of plasma dynamics with fluxes of energetic electrons. Particularly, the high intensity spike is launched at a time when the imploding shell may be sufficiently dense to stop the LPI-generated HEs. In that case, it is expected that the

additional energy from the HEs increases the ablation pressure[2,19]. Recent interpretations of strong shock experiments conducted on the PALS[20] and OMEGA[21] laser systems have demonstrated that the HEs may actually be detrimental to both the ablation pressure and the shock strength, while reinforcing the shock pressure and velocity[7,22].

Each of the processes involved in the compression of an ICF shell or in the shock modification by HEs fluxes can be studied separately[3,12,19,22,23]. However, the analysis of mutual effects requires an integrated tool designed for hydrodynamic scales. We investigate the effects of the Hot Electrons generated by the nonlinear laser-plasma interaction on the plasma dynamics of typical SI targets using the CHIC Lagrangian radiative hydrodynamics code[7,24]. In this description, the hydrodynamics is coupled to a model that consistently describes the linear LPI and the basic features of the non-linear LPI, including the generation of HEs by parametric instabilities and their propagation. This model is described in Sec. II and the framework of the study is given in Sec. III. For each target considered, we systematically analyse (i) the global implosion performance (with and without LPI-HEs), assessed by conducting a wide range of 2D simulations around their baseline design point in terms of ignitor pulse timing and power, and (ii) the detailed physical coupling between the LPI-HEs propagating into the target and the ignitor shock, the in-flight shell and the hotspot. First, we investigate in Sec. IV a pure-DT design from the HiPER project[25]. This target is expected to see its performances significantly degraded by the presence of LPI-HEs, as the DT is not an efficient material to stop the LPI-HE flux. Consequently, the latter does not contribute much to the ablation pressure but pre-heat the target. This provides a reference for the second target study presented in Sec. V, that of a DT target with a plastic ablator. The latter is more suited to stop the LPI-HE flux because of its higher ionization and areal density. As we will see, these targets do not ignite either for the design-point spike powers. In order to reach the ignition when considering the effects of the LPI-HE, we also study in Sec. V cases where the spike power is significantly increased. Finally, our conclusions are presented in Sec. VI.

II. MODELING

The state-of-the-art description of laser propagation on hydrodynamic scales relies on reduced approaches compatible with the performances of modern computers. The most common one is the Ray-Tracing model[26], that describes laser beams by bundles of needle-like rays following the Geometrical Optics (GO) propagation laws and characterized by a power density. In situations where collective effects and nonlinear couplings are unimportant ($I\lambda_L^2 \lesssim 5 \times 10^{13}$ Wμm^2/cm^2), GO-based models are sufficiently precise and computationally efficient. They

describe the laser refraction and plasma heating due to collisional energy absorption. Conversely, LPI modeling at higher interaction parameters requires knowledge of quantities such as the electric field amplitude and direction of the wavefront, which are not readily described by GO. In the model used here, the laser wavefield is described by stochastically distributed Gaussian optical beamlets[27] using the Paraxial Complex Geometrical Optics (PCGO)[28]. This approach allows to reproduce the main features of the intensity distribution of a large beam transformed by a Phase Plate. This knowledge of the laser intensity distribution and wavefield direction in plasma allows to model the main features of non-linear LPIs in a manner that is fully-coupled to the hydrodynamics and that is consistent in terms of laser energy conservation. This integrated model, briefly described in what follows, is also described in Refs. 7 and 27 and fully detailed in Ref. 29.

The PCGO model accounts for laser beam refraction, diffraction and linear inverse Bremsstrahlung absorption in the skin-depth at the critical density and in the under-dense corona. In addition, the LPI model accounts for the transfer of laser energy to supra-thermal electrons; at the critical density from the Resonant Absorption (RA), near the quarter critical density due to the TPD and below the quarter critical density due to the SRS. For each instability, the hot electron fluxes, average temperatures T_h, angular dispersion and direction are related with the laser intensity distribution (given by the PCGO beamlets) according to simplified expressions based on theoretical models and scaling laws obtained in kinetic simulations[7]. The energy transferred from the laser beams to the supra-thermal electrons is substracted from the corresponding PCGO beamlets at the point of HE emission, so that energy is naturally conserved in the model. The energy distribution of each individual HE beam is two-dimensional (2D) Maxwellian funciton $f_E(\epsilon) = \exp(-\epsilon/T_h)/T_h$, so that for a given average energy T_h, a significant amount of electrons also have energies above a few T_h. The HE beams propagation and energy deposition in plasma are described in the angular scattering approximation[30], adapted to 2D, transversally Gaussian, multigroup (2D Maxwellian) HE beams of arbitrary angular distribution. This model is implemented in the radiation hydrodynamics code and is resolved inline, thus accounting for (i) the competition for the laser energy between the various instabilities and with the linear collisional absorption, (ii) the coupling between nonlinear LPIs and plasma dynamics via the high energy electron beams and (iii) the losses due to backscattered SRS light. The model performance is confirmed by comparison with measurements of shock timing, laser absorption, HE fluxes and temperatures in SI experiments conducted on OMEGA[9,31] and PALS[5].

This study is limited to spherical implosions and thus the specific effects of CBET, that is mainly to alter the irradiation symmetry and decrease the laser-target coupling[27], are not included here. The eventual influ-
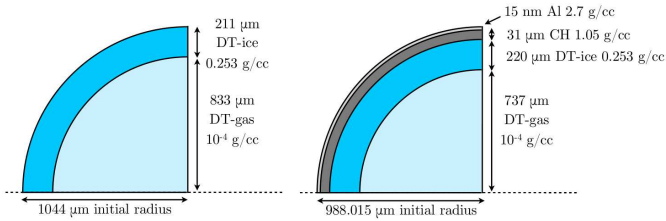
FIG. 1. Schematic of the two targets considered in the study. [left] Pure-DT target from the baseline HiPER project. [right] SI target with high yield and high safety margins with respect to the hydrodynamic instabilities and ignition windows.

ence of the coupling between CBET and LPI-HEs on the present results is discussed in the conclusion. Furthermore, the present model does not account for scattered light from the Stimulated Brillouin Scattering, that is not an issue for the present work focused on the effects of hot electrons on the implosion dynamics.

III. FRAMEWORK OF THE STUDY

A. Targets and geometry

Among known SI designs[4,25,32–36], two targets are considered: (i) the baseline pure-DT target proposed in the original HiPER project in Ref.[25] and (ii) an advanced design with increased gains and robustness to hydrodynamic instabilities, proposed in the CELIA laboratory. The latter target is more up-to-date with the current paradigms in direct-drive target design. Notably, it is imploded at a lower velocity ($\sim$ 245 km/s compared to $\sim$ 290 km/s for the pure-DT target) and features a plastic ablator for the reduction of hydrodynamic instabilities and optimization of laser-target coupling. The higher-Z ablator is also expected to provide a better absorption and control over the HE flux compared to the DT ablator. The targets are detailed in Fig. 1.

Each target is studied with two series of simulations, with and without the LPI-HE coupling. The simulations are conducted with the CHIC code in spherical geometry, with the SESAME Equation of States, radiative transport, DT reactions, α-particle heating and diffusion, and standard sharp cutoff of the electron thermal flux.

B. Laser configuration

The laser beams are in a direct-drive configuration relevant for a large-scale laser facility. We have assumed lasers of wavelength $\lambda_L = 351$ nm and a uniform irradiation field on the targets, with beams incident at an angle $\theta = 0$ with respect to the target normal. In both cases, the laser systems are supposed to be equipped with Kinoform Phase Plates. The corresponding intensity dis-
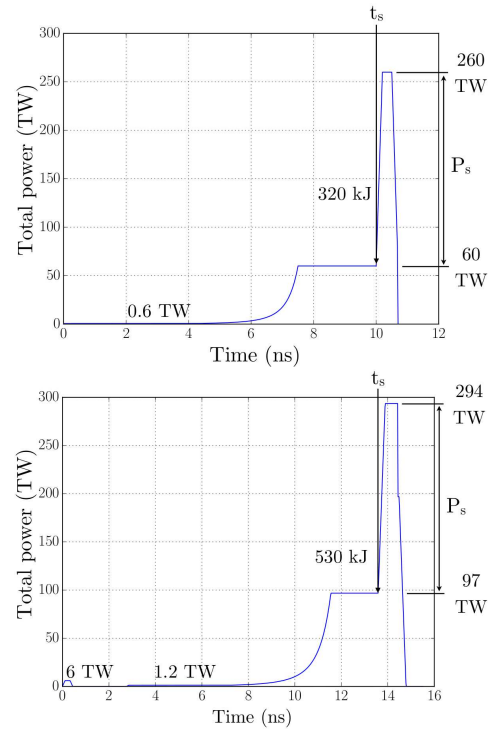

FIG. 2. Total pulse power used in the baseline designs of the [left] pure-DT and [right] CH-DT targets. For simplicity, it is considered that the irradiation geometry is uniform on the capsule and that each beam follows the same pulse shape, with the same focusing parameters.

tribution is modeled with PCGO using 100 beamlets per beam and by pseudo-randomly overlapping the beamlets in an interaction volume in which the speckle radius varies weakly[37,38]. Because the irradiation field is globally uniform and the beams are at normal incidence, the target dynamics only depends on the radial position r. However, in order to account for (i) the lateral scattering of LPI-generated HE beams, and (ii) the intensity distribution in plasma with PCGO, the simulations are conducted in 2D axially symmetric geometry instead of a purely 1D spherical geometry.

The baseline pulse shapes for both targets are shown in Fig. 2. We denote by t_s the time when the ignitor pulse is launched and by P_s the peak spike power, i.e. the addition to the laser power used for target compression (see Fig. 2). In the pure-DT target case, the pulse rise time is 200 ps, followed by a 300 ps high intensity plateau and a 200 ps fall time. In the baseline configuration, the 200 TW ignitor pulse is launched around $t_s = 10$ ns and the ignition occurs around 11 ns, for a total invested energy of $\sim$ 320 kJ and a yield of $\sim$ 24 MJ. In the CH-DT target case, the heavier capsule is imploded at lower velocities using a longer pulse. The 200 TW ignitor pulse is launched later, around $t_s = 13.5$ ns, with a 300 ps rise time, 600 ps plateau and 300 ps fall time. The ignition occurs around 14.6 ns, with a total invested energy of the order of $\sim$ 530 kJ and a yield of $\sim$ 45 MJ.
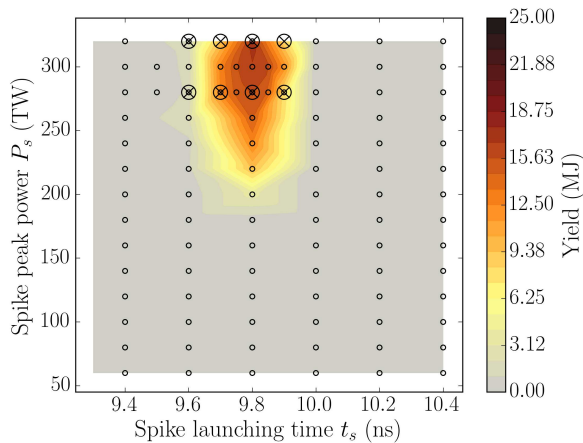
FIG. 3. (color) Target yield (MJ) of the pure-DT target, as a function of the spike launch time t_s and spike power P_s. Small circles indicate the points where the simulations with PCGO and without HEs were conducted. The large crossed circles represent equivalent simulations conducted with PCGO and the LPI-HE model, where no target ignition is attained.

IV. PURE-DT TARGET CASE

A. Ignition window

We conduct a set of reference simulations using PCGO without HEs, for $t_s \in \{9.4, 9.6, 9.8, 10, 10.2, 10.4\}$ ns and P_s varying in the $[60; 320]$ TW interval. These simulations are conducted with the flux limiter value of $f_L = 0.04$ in agreement with experimental validations of the CHIC code with PCGO presented in Ref.[7]. The resulting ignition window is shown in Fig. 3. The spike launch times and target yields are in good agreement with computations realized in 1D[3,10] with a standard Ray-Tracing model[26]. The higher spike power obtained in our simulations (compared to what is presented in the literature) is related to the choice of a rather low flux limiter value $f_L = 0.04$ compared to the baseline value $f_L = 0.06$ used initially for the design of the HiPER target.

Various simulations are conducted with PCGO including the LPI-generated HEs. Anticipating that the presence of HEs (i) should increase the shock velocity, so that the ignitor shock should be launched later to obtain a similar shock entry time into the hotspot compared to the reference case, and (ii) may slightly decrease the convergence ratio of the shell, so that one should launch the ignitor shock earlier to compensate the earlier shell stagnation time, we have chosen $t_s = \{9.6, 9.7, 9.8, 9.9\}$ ns. Note that the most robust timing without HEs is $t_{s,\mathrm{opt}} \simeq 9.8$ ns. We consider two values for the spike power: $P_s = \{280, 320\}$ TW. Neither of these simulations with LPI-HEs predict the target ignition. To understand the reason for that, we discuss the processes at play in these implosions by comparing the particular case
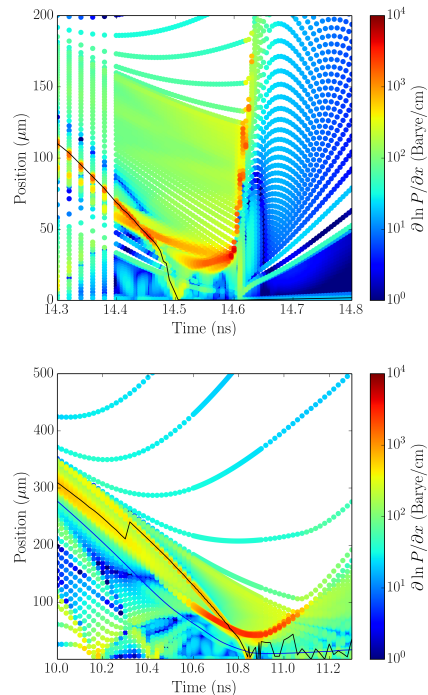

FIG. 4. (color) Flow diagrams (logarithmic pressure gradient, shown in log-scale) of the targets as a function of time and radial coordinate, for the case [top] without LPI-HEs, and [bottom] with the LPI-HEs, and for $t_s = 9.8$ ns and $P_s = 320$ TW. The position of the strongest shock is indicated as a black line, and the position of the initial DT-ice/DT-gas interface as a blue line. Oscillations in the shock position after the shock collapse are due to the uncertainty in detecting numerically the shock position. Each dot indicates the position of a Lagrangian mesh cell.

of $t_s = 9.8$ ns and $P_s = 320$ TW, with and without LPI-generated HEs. The target yield in this case is of ~ 10.25 kJ with the LPI-HEs and 16.9 MJ in the reference case.

The global target dynamics is illustrated in Fig. 4, which shows the logarithmic pressure gradient as a function of the target radius and time. Several observations can be readily made from these diagrams: (i) the target with LPI-HEs does not ignite, (ii) the in-flight thickness of the imploding shell increases in the case with LPI-HEs, (iii) the final convergence ratio is lower with HEs, (iv) the ignitor shock reaches the target center earlier in the case with HEs and (v) the shock strength appears higher without HEs than with HEs. Note that in the case with HEs, the ignitor shock collapse time evoked in point (iv) is closer to the shell stagnation time because the shell convergence ratio is lower. This is accounted for in the simulations with an earlier spike launch time with HEs, which does not reach ignition either, as indicated in Fig. 3. We now detail the above-mentioned points more precisely.

B. Shell preheat

In the simulations, the SRS, TPD and RA processes emit copious amounts of electrons at averaged temperatures of $\sim$ 41 keV, 100 keV and 2.7 keV, respectively, with the total energies of $\sim$ 1.38 %, 0.97 % and 0.33 % of the total laser energy, respectively (see Fig. 5 [top-right] for an example of the corresponding HE distribution in plasma at various times). During the spike plateau, about 13% of the hot electrons have energies above 125 keV, mostly from TPD. Given the initial divergence of TPD-generated HEs and the distance between the quarter-critical density and the in-flight shell, at least half of the TPD-HEs reach the shell during the implosion. The time-history of the instantaneous HE fluxes (normalized to the incident laser intensity) is shown in Fig. 5, alongside the corresponding HE spectra and the shell areal density $(\rho R)_{\mathrm{HE}}$ seen by the LPI-HEs, at various times. The latter is defined as:

$$(\rho R)_{\mathrm{HE}}(r) = \int_r^{r_{n_c/4}} \rho(r')\mathrm{d}r' \tag{1}$$

where r is the radial coordinate and $r_{n_c/4}$ is the coordinate of the quarter critical density. The areal density required to stop a mono-energetic electron beam of a given energy propagating in a constant density DT plasma[39] is shown in Fig. 5 [bottom-right]. This panel provides an estimate of the HE energies that can be stopped by the shell. Given the HE energies involved here, and the shell areal densities reported in Fig. 5 [bottom-left], we see that the shell is not dense enough to stop the higher part of the HE spectrum. Notably, at the begining of the spike plateau, the in-flight shell can be integrally heated by the electrons with the energies above $\sim$ 125 keV. Nearing the end of the plateau, the electrons with energies above 170 keV still preheat the shell. Considering the significant amount of high-energy electrons generated by the SRS and TPD, the shell is preheated in the bulk, as is shown in Fig. 6.

In the SI experiments on Pals and Omega presented in Refs.[5,7,8], the target preheat from LPI-generated HEs occurred in the bulk of a target of quasi-uniform solid density. In the case of a SI-ICF target, the preheat occurs in a shell surrounded by lower density regions on either sides. Consequently, the pressure increase induced by the HE preheat does not occur at a constant density. The preheat causes the global expansion of the shell: its thickness and temperature increase in-flight while its density decreases. This is illustrated in Fig. 7 [top]. The increase in the shell pressure raises its adiabat α while it converges to the center, as shown in Fig. 7 [bottom]. The increase of α leads to the lower convergence ratios seen in Fig. 4, from $C_R \approx 833/24.1 = 34.6$ without HEs to $C_R \approx 833/30.4 = 27.4$ with HEs. It can also be noted from Fig. 7 [top] that the expansion of the inner shell boundary due to the preheat can be considered as an inner ablation leading to contamination of the hot spot by the cold shell material. It effectively causes an increase in the density of the target center. This HE-induced hotspot mass increase is also discussed later in this section while considering the thermodynamic path of the hotspot.

C. Shock characteristics

The shock created by the high intensity ignitor pulse propagates through the preheated material while its temperature and pressure increases, and its density decreases (see Fig. 7 [top]). The resulting pressure and temperature downstream of the shock are shown in Fig. 8 [top] alongside its position. We see that for a same launching time t_s, (i) the shock is faster with HEs, (ii) it reaches the hotspot with a pressure of $\sim$ 30 GBar for the case with HEs and $\sim$ 10 GBar for the case without HEs, and (iii) the post-shock temperature at this time is twice higher in the case with HEs. As was observed in the interpretation of recent SI experiments[7], the HEs significantly increase the shock pressure. This increase is not due to an increased ablation pressure, the latter being slightly lower with HEs as shown in Fig. 8 [bottom-left], but to the plasma preheat upstream of the shock, that can be clearly seen in Fig. 7 [bottom]. Finally, the shock strength is smaller with HEs, as shown in Fig. 8 [bottom-right] and in agreement with the previous conclusions of interpretation on strong shock experiments[7].

D. Hotspot thermodynamic path

We have seen that the ignitor shock is propagating with a larger post-shock pressure, a lower strength and a higher velocity when considering the LPI-HEs. We now assess the characteristics of the hotspot in order to determine how the shock deposits its energy and why the target does not reach the ignition. The evolution of the hotspot characteristics is assessed in a $(\rho R, T)$ diagram. The hotspot averaged areal density $\langle \rho r \rangle_H$ and averaged temperature $\langle T_H \rangle$ are defined as:

$$\langle \rho r \rangle_H = \int_0^{R_H} \rho(r)\mathrm{d}r , \tag{2}$$

$$\langle T_H \rangle = \frac{3}{R_H^3} \int_0^{R_H} r^2 T_i(r)\mathrm{d}r , \tag{3}$$

where R_H is the hotspot radius, defined as the radial coordinate r where $T_i(r) = T_i(0)/10$, with $T_i(0)$ being the ion temperature in the target center. Note that the angular coordinate does not appear here: the simulation being monomode the plasma parameters only depend on the radial position. The thermodynamic path of the hotspot for the case with and without HEs is shown in Fig. 9. As evoked earlier, the simulation without HEs reaches the ignition boundary (shown with a dashed line), while the simulation with HEs does not. The most notable difference is the areal density in the case with HEs that is
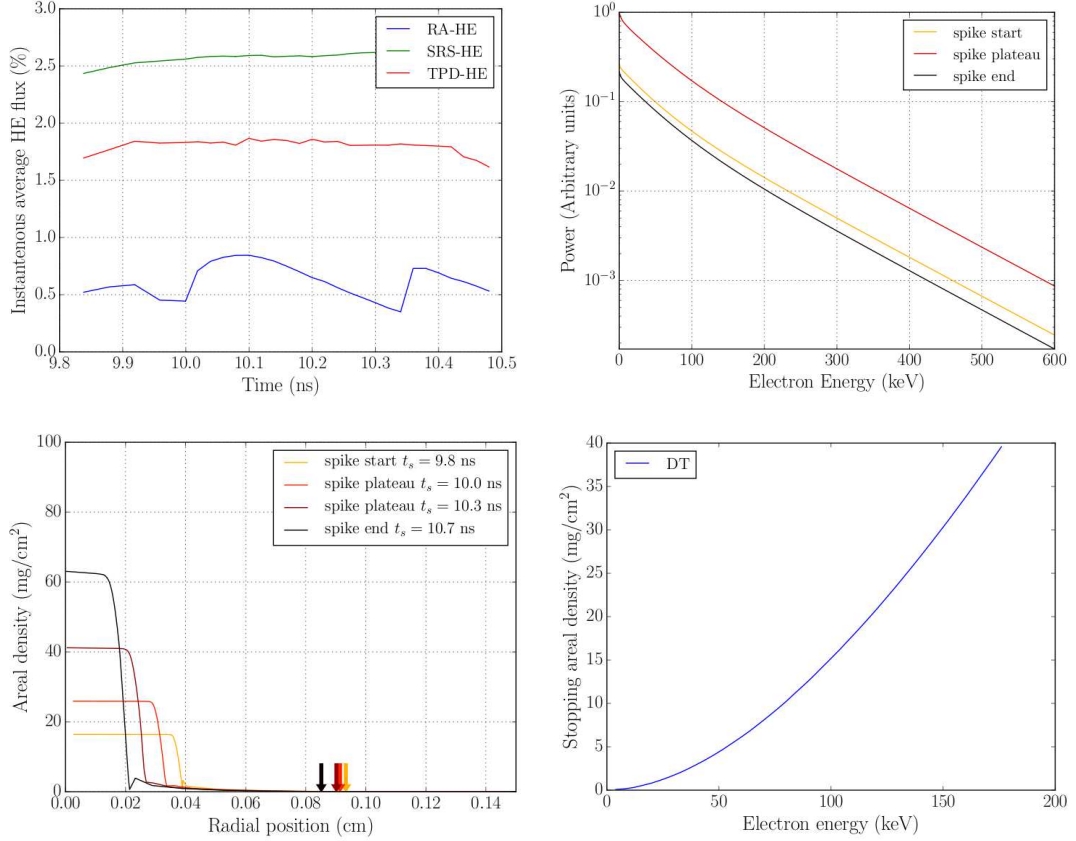
FIG. 5. (color) [top-left] Flux-weighted averages of the laser to HE instantaneous energy conversion fractions. The spectra of HEs accelerated in plasma are shown in the [top-right] panel, considering the beginning of the laser spike in orange (light grey), the plateau of the spike in red (grey) and the end of the laser spike in black. [bottom-left] Areal density $(\rho R)_{\mathrm{HE}}$ seen by the HE beams emitted at $n_c/4$, as a function of the target radius. The position of the quarter critical density is indicated by an arrow. [bottom-right] Estimate of the areal density required to stop a mono-energetic electron beam of a given energy propagating in a homogeneous DT plasma of temperature 1 keV[39]. These electron ranges vary weakly for plasma temperatures from 100 eV to a few keV.
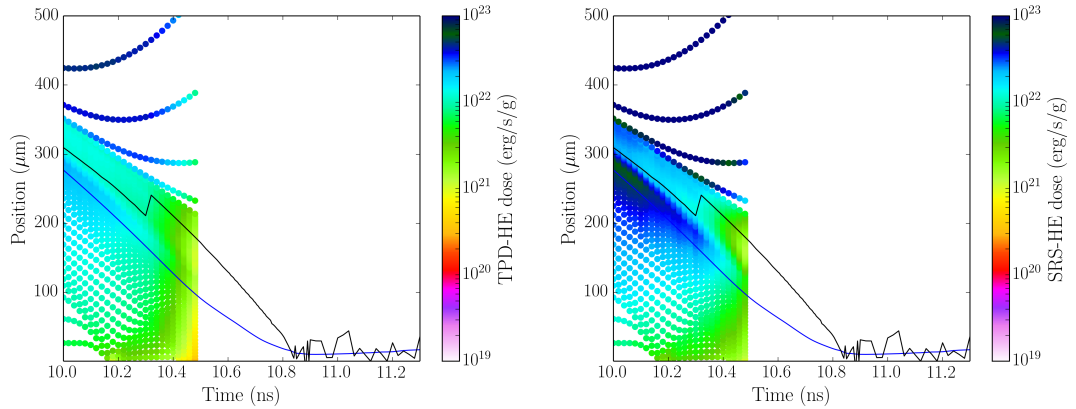

FIG. 6. (color) Log-scaled dose deposited by the HE beams in plasma (erg/s/g), as a function of the target radius and time. [left] HE generated by the TPD and [right] by the SRS (the simulation being monomode, the fields presented here are identical for any cylindrical angle θ). Each dot indicates the position of a Lagrangian mesh cell.

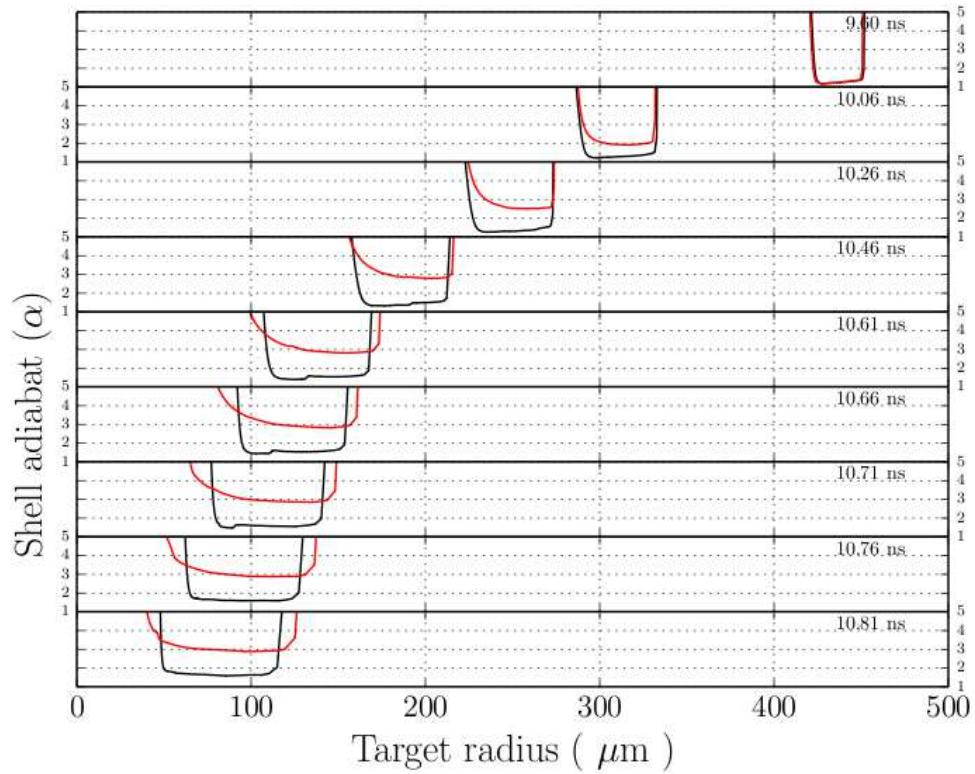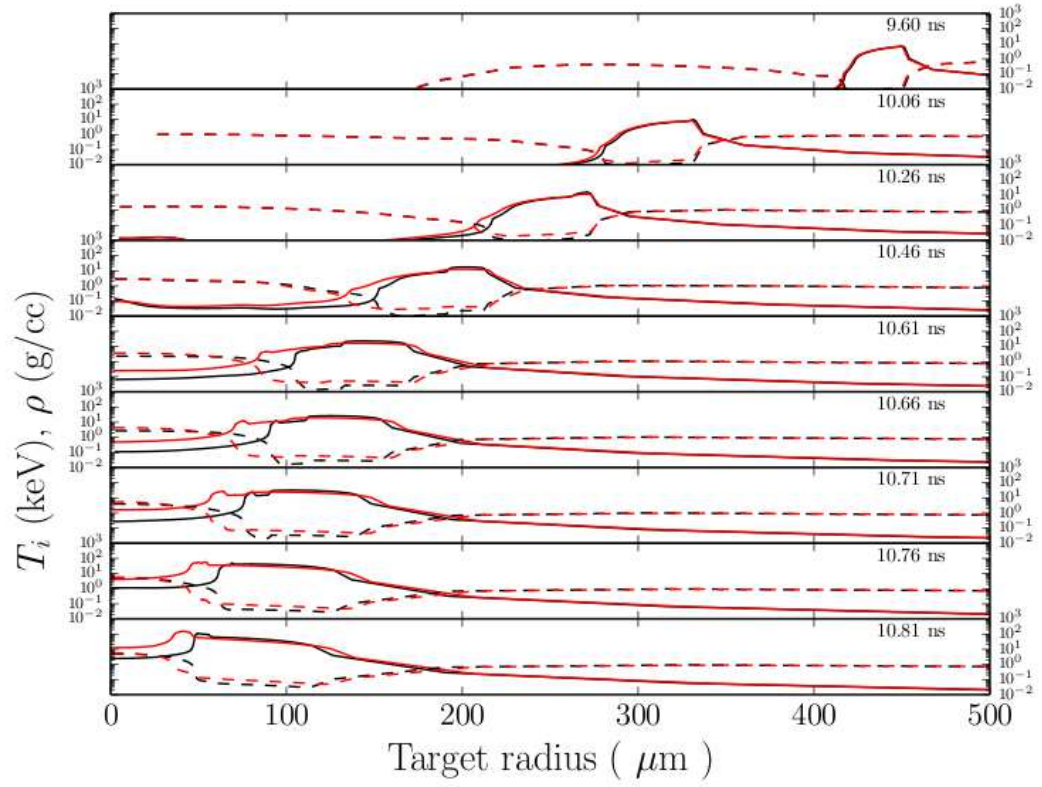FIG. 7. (color) [top] Slices of plasma density ρ (in g/cc) indicated by plain lines, and ion temperature T_i (in keV) indicated by dashed lines, and [bottom] slices of the adiabat parameter α, as a function of the target radii and for various times indicated on the upper-right corner of each subplot. Results from the simulation without HEs are shown in black and with HEs in red (grey).
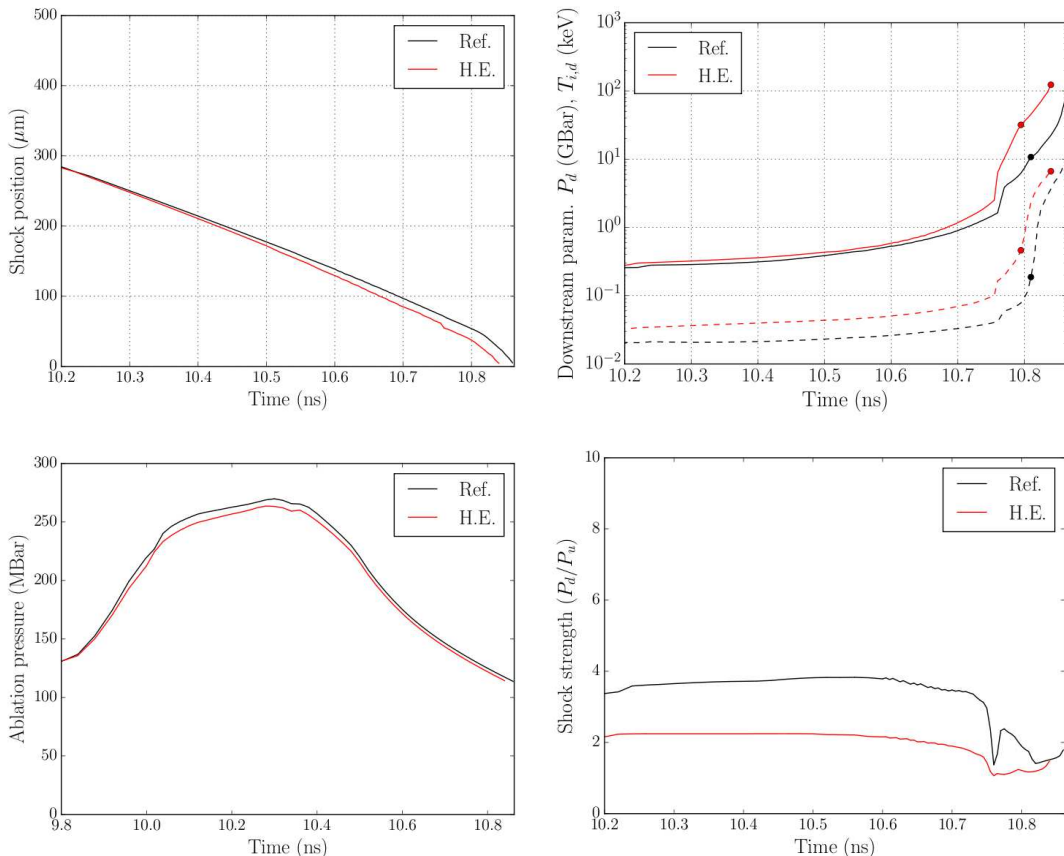
FIG. 8. (color) [top-left] Position of the strongest shock in the material. [top-right] Temperature (keV) and pressure (GBar) of the shocked plasma. The plain line indicates the downstream shock pressure and the dashed lines the downstream shock temperature. For each curve, the first circle represents the time when the shock enters into the hotspot, and the second circle indicates the time when the shock reaches the target center. [bottom-row] Time histories of [bottom-left] the ablation pressure and [bottom-right] the ignitor shock strength. For all panels, black and red (grey) curves indicate simulation results without and with HEs, respectively.

significantly higher when the shock reaches the hotspot (first dot in Fig. 9). This increase in hotspot density originates from the ablation from the inner shell surface preheated by the HEs, as shown in Fig. 7 [top]. The slight increase in temperature at this time is due to the smaller hotspot radius. For clarity, the properties of the hotspot at the time of shock entry and shock rebound are given in Tab. I.

1. Hotspot mass

The hotspot mass M_h can be expressed as:

$$M_h = \frac{4}{3}\pi \frac{(\rho_h R_h)^3}{\rho_h^2} \approx \frac{4}{3}\pi \frac{\langle\rho r\rangle_H^3}{\langle\rho_H\rangle^2} \ . \qquad (4)$$

Although the hotspot areal density is higher with HEs (as shown in Fig. 9) it also has a higher density (as seen in Fig. 7 [top]), so that the overall hotspot mass M_h is higher in the simulations with HEs. The time evolution

of the hotspot mass is shown in Fig. 10, alongside the shock position and the radius of the hotspot. At the time when the shock reaches the target center, its mass is of 2.65 μg and 10.7 μg for the cases without and with HEs, respectively. The energy E_h required to bring a DT sample of mass M_f to a temperature T_h can be estimated from the expression for its internal energy[40]:

$$E_h \approx 110 M_f T_h \ \mathrm{MJ} \ , \qquad (5)$$

where M_f is expressed in g and T_h in keV. This equation shows that in order to heat the DT fuel to a given temperature (typically $\sim$ 7 keV is required to ignite a hotspot of areal density of 0.2 g/cm^2), the increase in hotspot mass translates into an increase in required energy. Although we have seen that the shock downstream pressure is higher with HEs, it is not sufficient to ignite the hotspot of significantly increased mass (as seen in the thermodynamic diagram). Indeed, the temperature of the hotspot barely increases between the time when the shock propagates from the hotspot radius $r = R_h$ to the target center $r = 0$.

shock position	case	$\langle \rho r \rangle_H$	$\langle T_H \rangle$	$\langle \rho_H \rangle$	R_H	$\langle T_{H,e} \rangle$
inner shell edge	no HE	0.016 g/cm^2	2.5 keV	4.63 g/cc	48.7 μm	2.05 keV
	LPI-HE	0.048 g/cm^2	2.7 keV	16.93 g/cc	40.2 μm	2.53 keV
target center	no HE	0.063 g/cm^2	3.95 keV	22.17 g/cc	30.52 μm	3.52 keV
	LPI-HE	0.14 g/cm^2	2.88 keV	65.9 g/cc	33.63 μm	2.75 keV

TABLE I. Summary of the properties of the hotspot when [top] the ignitor shock enters into the hotspot and [bottom] the ignitor shock reaches the target center. $\langle \rho_H \rangle$ is the averaged hotspot density and $\langle T_{H,e} \rangle$ is the averaged hotspot electron temperature. Both quantities are computed using the same averaging process as for the ion temperature (Eq. (3)). Note that because of these definitions, $\langle \rho_H \rangle R_H \neq \langle \rho r \rangle_H$.
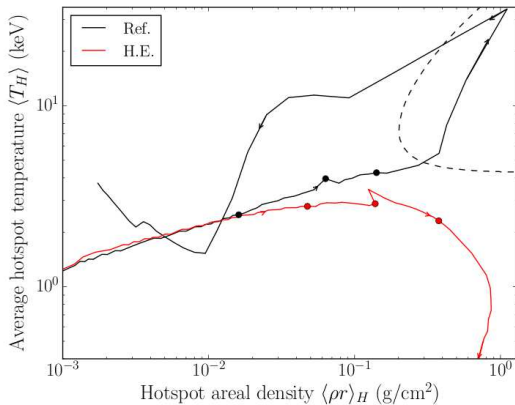

FIG. 9. (color) Thermodynamic path of the hotspot, for the case without LPI-generated HEs in black and with the LPI-HE model in red (grey). The isobaric ignition curve is shown as a dashed line[3]. Arrows indicate the direction of the temporal evolution of the hotspot. For each curve, the first dot indicates the time when the ignitor shock enters into the hotspot, the second indicates the time of shock rebound on the target center and the third is the time when the shock collides with the inner surface of the shell.
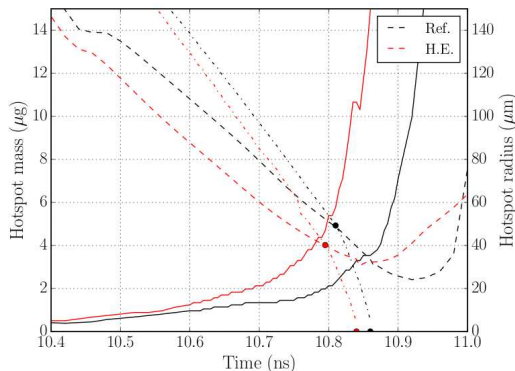

FIG. 10. (color) Mass of the hotspot as a function of time, indicated as plain lines. The hotspot radius is shown as dashed lines and the shock position as dotted dashed lines. The times when the shock enters into the hotspot and reaches the target center are indicated by colored circles. Data from the simulation without HEs and with HEs are shown in black and red (grey), respectively.

2. Hotspot power balance

As it is shown in Fig. 9, by the time the shock rebounds and reaches the shell again, the hot spot temperature has decreased. This is indicative of intense hotspot cooling, i.e. power losses are higher than the power brought in by the ignitor shock. We now assess the importance of these cooling processes. The hotspot can loose its energy either by the electron thermal conduction or by the radiative losses from the Bremsstrahlung process. The hotspot power density $\mathcal{W}_e$ lost through electron thermal conduction can be estimated by[40]:

$$\mathcal{W}_e = 1.71 \kappa_0 \frac{T_h^{7/2}}{R_h^2} \ , \qquad (6)$$

where the constant value $\kappa_0 = 3 \times 10^{12}$ W/cm/keV$^{7/2}$ corresponds to the Spitzer-Härm thermal conductivity. At the time when the shock enters into the hotspot and using the values given in Tab. I, we find that hot electrons increase the electron conductivity losses by a factor of three, $\mathcal{W}_{e,\mathrm{HE}} \approx 3\mathcal{W}_{e,\mathrm{ref}}$. Similarly, the hotspot power density $\mathcal{W}_B$ lost through the radiative process can be estimated by[40]:

$$\mathcal{W}_B = C_B \rho_h^2 T_h^{1/2} \ , \qquad (7)$$

where $C_B = 3 \times 10^{16}$ W cm^3/keV$^{1/2}$/g^2. At the time when the shock enters into the hotspot and using the values given in Tab. I, we find that the radiation losses increase by a factor of 15, $\mathcal{W}_{B,\mathrm{HE}} \approx 15\mathcal{W}_{B,\mathrm{ref}}$. The total power loss $\mathcal{W} = V_h \mathcal{W}$ can be estimated by using the hotspot volume $V_h = (4/3)\pi R_h^3$. We compare in Tab. II the power losses at the time when the shock enters into the hotspot and reaches the target center.

The hotspot density increase induced by the HE preheat of the shell and its inner side ablation lead to an increase of radiative losses by an order of magnitude. Using the value for $\mathcal{W}_{B,\mathrm{HE}}$ at the time of shock rebound and assuming a constant power loss for 30 ps, one finds that the hotspot looses ~ 1 kJ of energy. Assuming a hotspot mass of 20 μg, it follows from Eq. (5) that this corresponds to a temperature decrease of 0.5 keV. Even though the ignitor shock produces an enhanced downstream pressure in the case with HEs, the latter is unable

	inner shell edge		target center	
case	$\mathcal{W}_B$ (TW)	$\mathcal{W}_e$ (TW)	$\mathcal{W}_B$ (TW)	$\mathcal{W}_e$ (TW)
no HE	0.45	0.13	3.36	0.54
LPI-HE	3.8	0.229	35.1	0.25

TABLE II. Power lost by the hotspot from the processes of Bremsstrahlung and electron thermal conduction. Values are given for the time when [left] the ignitor shock enters into the hotspot and [right] the ignitor shock reaches the target center.

to compensate for the (i) ten-fold increase in radiation losses and (ii) the additional hotspot mass that must be heated. Consequently, the post temperature $T_P \sim 4.3$ keV, at which the α particle production compensates the radiative losses, is never reached.

These conclusions explain the failed ignition in the simulations of the reference target and provide a basis for the analysis of the case of the CH-DT target.

V. CH-DT TARGET CASE

A. Ignition window

We now consider the dynamics of the CH-DT target, detailed in Sec. III, in the absence and presence of the LPI-HEs. Given the higher average charge state in the CH shell, this target was originally designed with a flux limitation f_L of 7 % to account for the lower electron heat conductivity. The resulting increased laser absorption allows one to decrease the spike power required to reach ignition (which are lower than in the pure-DT case). For consistency with this design point, the flux limiter in this section is set to $f_L = 0.07$. The reference simulations without HEs are made for the spike launch time in the interval $t_s \in [13; 13.6]$ ns and P_s varying from 20 to 220 TW. Given the slightly smaller radius of the CH-DT target, the laser intensity is rather similar compared to the pure-DT case and the laser-plasma interaction proceeds in a comparable regime.

The reference ignition window (without HEs) is shown in Fig. 11 [left]. It is in reasonable agreement with the baseline computations realized in the 1D spherical geometry with the Ray-Tracing model in CHIC. Simulations conducted with LPI-generated HEs model are presented in Fig. 11 [middle] for comparable spike powers. The targets do not reach ignition in this $[t_s; P_s]$ range. This is not a shock mis-timing issue, as the neutron maximum curve is correctly bracketted, as shown by the blue curve in Fig. 11 [middle]. Compared to the pure-DT target, the yields in these non-igniting cases are higher by a few orders of magnitude up to a fraction of MJ, indicating higher fusion reaction rates despite the presence of LPI-HEs. Higher spike power cases are presented in Fig. 11 [right], up to 500 TW peak power. In these cases, the target ignition is reached in presence of the LPI-HEs, with

three quarters of the yield of the reference case without LPI-HEs.

The target dynamics analysis is separated in two parts. First, we focus in Sec. V B on the $P_s \in [0; 300]$ TW interval with and without LPI-generated HEs. Second, we present in Sec. V C the simulation results using higher spike powers $P_s \in [450; 500]$ TW.

B. Nominal power cases

In order to analyze the target dynamics in the nominal power cases, we focus on simulations conducted at the most robust shock launching time of $t_{s,\mathrm{opt}} = 13.30$ ns, that lies in the middle of the reference ignition window (Fig. 11 [left]). This timing also corresponds to the maximum neutron production for the cases with LPI-HEs and nominal power. For this value of $t_{s,\mathrm{opt}}$, the spike power required to reach the ignition without HEs is of ~ 80 TW. We study the effects of HEs by comparison with the particular design point without HEs of $P_s = 200$ TW. We consider three simulations with LPI-HEs and the spike launching time $t_s = 13.30$ ns: (i) a *nominal case* with $P_s = 200$ TW, (ii) a *medium power case*[41] with $P_s = 300$ TW, and (iii) a *non-stationary case* where we consider that the nonlinear LPIs requires 200 ps in order to reach a steady state, as was observed in Shock Ignition experiments[9]. In that case, the 200 TW spike is still launched at $t_s = 13.30$ ns, but the HEs are launched at $t_{\mathrm{HE}} = t_s + \Delta t_{\mathrm{HE}} = 13.50$ ps (this particular simulation is not indicated in Fig. 11). This non-stationary case is insightful but may not be realistic: although a transient phase where the SRS and TPD did not accelerate HEs was observed in spherical experiments of Shock Ignition[8,9], this delay was explained by a small overall energy and small target size, leading to steep density gradients and relatively high SRS/TPD thresholds. The scales of plasma considered here and the ignition targets are much larger, and hence much more prone to the SRS and TPD instabilities.

1. Hot Electron fluxes and target preheat

In the nominal simulation with $P_s = 200$ TW, the SRS, TPD and RA processes produce high energy electrons at averaged temperatures of ~ 43 keV, 98 keV and 1.4 keV, respectively, with total energies of ~ 1.2 %, 0.94 % and 0.12 % of the total laser energy, respectively. These values are reported for all cases in Tab. III. Mainly, the total HE energy increases significantly with the laser intensity, as both the instantaneous HE fluxes and the incident laser power (to which the HE fluxes are normalized) increase. The increase of the HE temperature with the laser intensity is less prominent. Note that the average temperature of the TPD-HE distributions is limited to 100 keV maximum in the model[42], that is already saturated at the lowest spike power settings. The time-
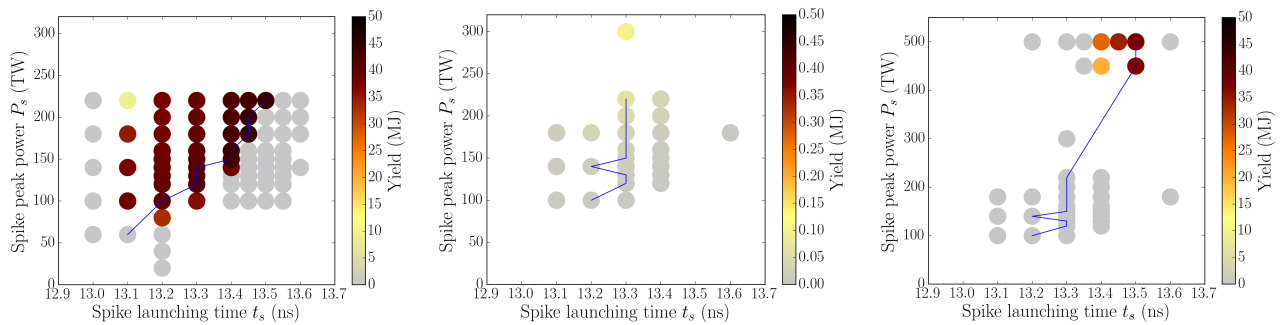
FIG. 11. (color) Target yield (MJ) of the CH-DT target, as a function of the spike launch time t_s and spike power P_s. Circles indicate the spike parameters where the simulations were conducted. Simulation results [left] with PCGO and without HEs and [middle,right] with PCGO and LPI-generated HEs. The values shown on the [middle] graph are centered on the same ignitor spike powers P_s as the reference graph on the [left], and with a reduced yield range (up to 0.5 MJ instead of 50 MJ). The values shown on the [right] graph are simulation results up to 500 TW ignitor spike powers with the full yield range. The blue curves indicate the position of the maximum neutron production for a given spike power.

case	P_s	t_s	$\langle I_{\text{peak}}^{r_{n_c}} \rangle$	$\mathcal{F}_{\text{RA}}$	$\mathcal{F}_{\text{SRS}}$	$\mathcal{F}_{\text{TPD}}$	$\langle T_{h,\text{RA}} \rangle$	$\langle T_{h,\text{SRS}} \rangle$	$\langle T_{h,\text{TPD}} \rangle$
nominal	200 TW	13.30 ns	7.56×10^{15} W/cm^2	0.12 %	1.2 %	0.94 %	1.4 keV	43 keV	98 keV
delayed HEs	200 TW	13.30 ns	7.56×10^{15} W/cm^2	0.11 %	1.05 %	0.84	1.5 keV	43.4 keV	98.9 keV
medium power	300 TW	13.30 ns	1.01×10^{16} W/cm^2	0.18 %	1.37 %	1.1 %	1.93 keV	44.5 keV	99 keV
high power	500 TW	13.30 ns	1.53×10^{16} W/cm^2	0.29 %	1.6 %	1.33 %	2.98 keV	46.4 keV	99 keV

TABLE III. Averaged parameters of the hot electrons accelerated into the target. $\langle I_{\text{peak}}^{r_{n_c}} \rangle$ is the peak total laser intensity (spike + compression) at the start of the ignitor spike plateau, estimated at the critical density radius r_{n_c} by $P/(4\pi r_c^2)$. The fluxes $\mathcal{F}$ are expressed in percent of the total incoming laser energy. At a given time, the fluxes $\mathcal{F}$ and average temperature of the HE distribution T_h are spatially averaged over all the HE sources defined by the LPI-HE model. The fluxes are then integrated over the laser duration, and the temperatures are averaged using a mean weighted with the fluxes. The high power case, analyzed in Sec. V C, is also given for comparison.

history of the instantaneous HE fluxes are shown in Fig. 12, alongside with the corresponding HE spectra and the shell areal density at various times.

The instantaneous fluxes and spectra are similar to those predicted in the pure-DT case. Compared to the latter, the areal density is approximately twice higher in the DT shell, because of higher initial density and the enhanced target convergence. Although the plastic has a higher capacity to stop high energy electrons because of its higher Z (the range of electrons in CH is given in Fig. 12 [bottom-right]), the low areal density of the ablator makes it unable to stop HEs of energies larger than 50-70 keV. However, the ablator still stops a significant amount of the low energy electrons, thus partially protecting the in-flight shell, which final convergence is unaltered by the presence of LPI-HEs. The electrons of higher energies propagate in the compressed DT shell, which reaches areal densities of 40-100 mg/cm^2 during the laser spike plateau. This represents a capacity to stop electrons of energies up to 170 keV at the beginning of the spike plateau. As such, this target is significantly more resiliant to the LPI-generated HEs in general. The bulk of the DT shell is preheated by these higher energy electrons (between 70 and 170 keV), but at lower fluxes

(see Fig. 12 [top-right]). A more significant portion of the spectrum is stopped in the plastic and in the outer region of the in-flight DT shell. Note that when launching the HEs 200 ps later than the pulse start, the shell areal density has increased by ~ 20 %.

The magnitude of the DT bulk preheat can be assessed in the temperature, density and adiabat parameter profiles shown in Fig. 13. Overall, the target dynamics in the two 200 TW cases with HEs are rather similar so that the 200 ps delayed-HE case will not be shown in figures for clarity. The hotspot density increases with the dense shell material, that can be seen in Fig. 13 [top], is the least severe for the delayed-HE case, then for the nominal case, and is the most severe for the 300 TW power case (this is easily seen at $t = 14.20$ and 14.40 ns). This density increase is correlated with a hotspot mass increase, as illustrated in Fig. 14, and a slight hotspot temperature decrease due to the cold mass flux and compensated by the hotspot preheat. Compared to the pure-DT target, the shell conserves a more cohesive structure, i.e. it is closer to the reference case without HEs. This is correlated with a lower shell preheat in general than in the pure-DT case. This can notably be seen in the profiles of the adiabat parameter α shown in Fig. 13 [bottom].
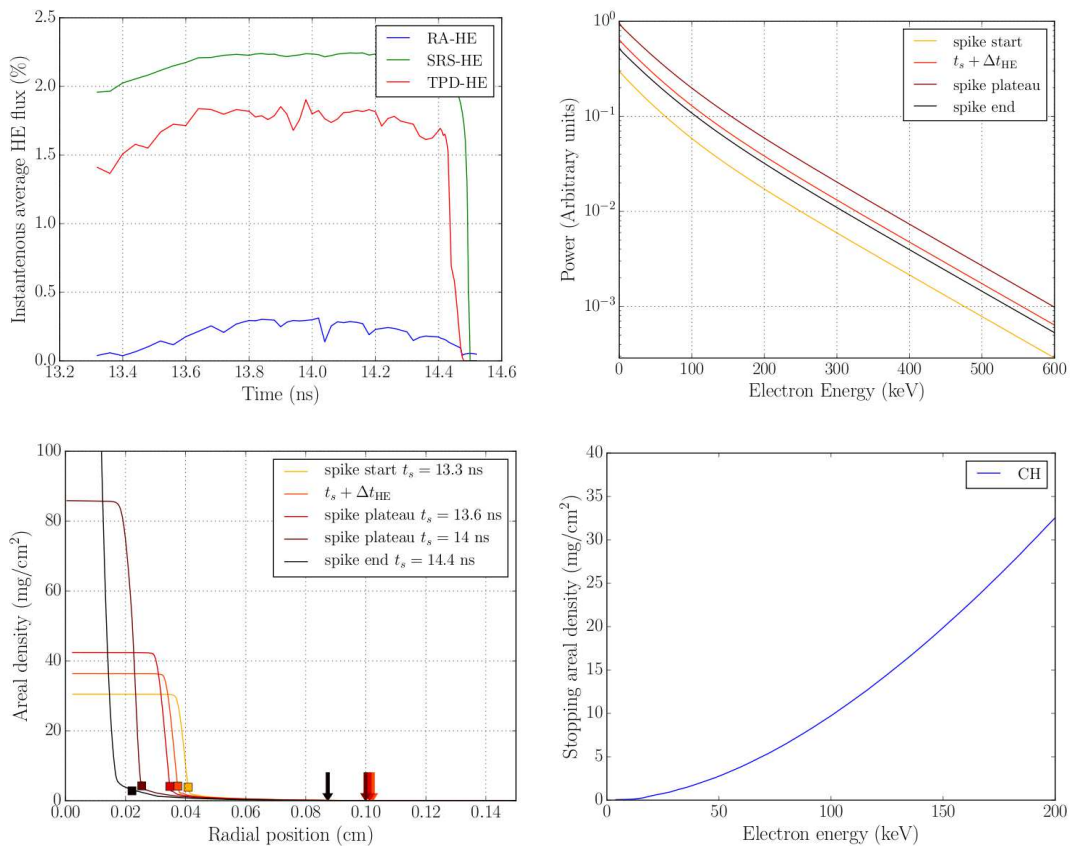
FIG. 12. (color) [top-left] Flux-weighted averages of the instantaneous laser to HE energy conversion fractions. The spectra of HEs accelerated in plasma are shown in the [top-right] panel, considering the beginning of the laser spike in orange (light grey), the plateau of the spike in bright red and dark red (grey) and the end of the laser spike in black. [bottom-left] Areal density seen by the HE beams emitted at $n_c/4$, as a function of the target radius. The position of the quarter critical density is indicated by an arrow. The position of the DT-ice/CH interface is indicated by a square. Simulations results for these plots are from the nominal power case. [bottom-right] Estimate of the areal density required to stop a mono-energetic electron beam of a given energy propagating in a homogeneous CH plasma[39]. These electron ranges vary weakly for plasma temperatures from 100 eV to a few keV.

The adiabat parameter is close to 2 at the peak convergence, lower for the delayed-HE case and higher for the 300 TW power case. Even for the latter configuration, the parameter α reaches the value of 2.3. That is smaller than the value of 3 observed in the pure-DT case with HEs, which confirms that the plastic ablator did stop a significant portion of the LPI-HE spectrum.

2. Shock characteristics

The properties of the shock created by the ignitor pulse are shown in Fig. 15. The position of the shock is shown in the [top-left] panel. Here, the shell preheat is less significant than in the pure-DT case, so that the shock velocity is less affected by the presence of LPI-HEs. For a same incident laser power P_s, the presence of the HEs slightly delays the shock convergence time because the ablation pressure is lower (see [bottom-left] panel). In the case with increased power, the shock reaches the tar- get center earlier, owing to a larger ablation pressure. The plasma properties downstream of the shock are indicated in the [top-right] panel, and the shock strength is shown in the [bottom-right] panel. The downstream shock temperature is similar in all cases. For a same shock launching time and ignitor spike power, the downstream shock pressure is higher in presence of LPI-HEs, although less significantly than in the pure-DT case, owing to the decreased shell preheat. This highlights that when shielding the target with respect to LPI-HE, one also looses the advantage of shock pressure amplification due to the preheating. Overall, the shock strength is the highest in the reference case. The increased ablation pressure in the 300 TW LPI-HE with respect to the 200 TW cases compensates the increased shell preheat (that otherwise tends to decrease the shock strength), so that the overall shock strength in the LPI-HE cases is the highest for $P_s = 300$ TW. Considering the LPI-HE 200 TW cases only, the preheat is less significant in the delayed-HE case, leading to a higher shock strength
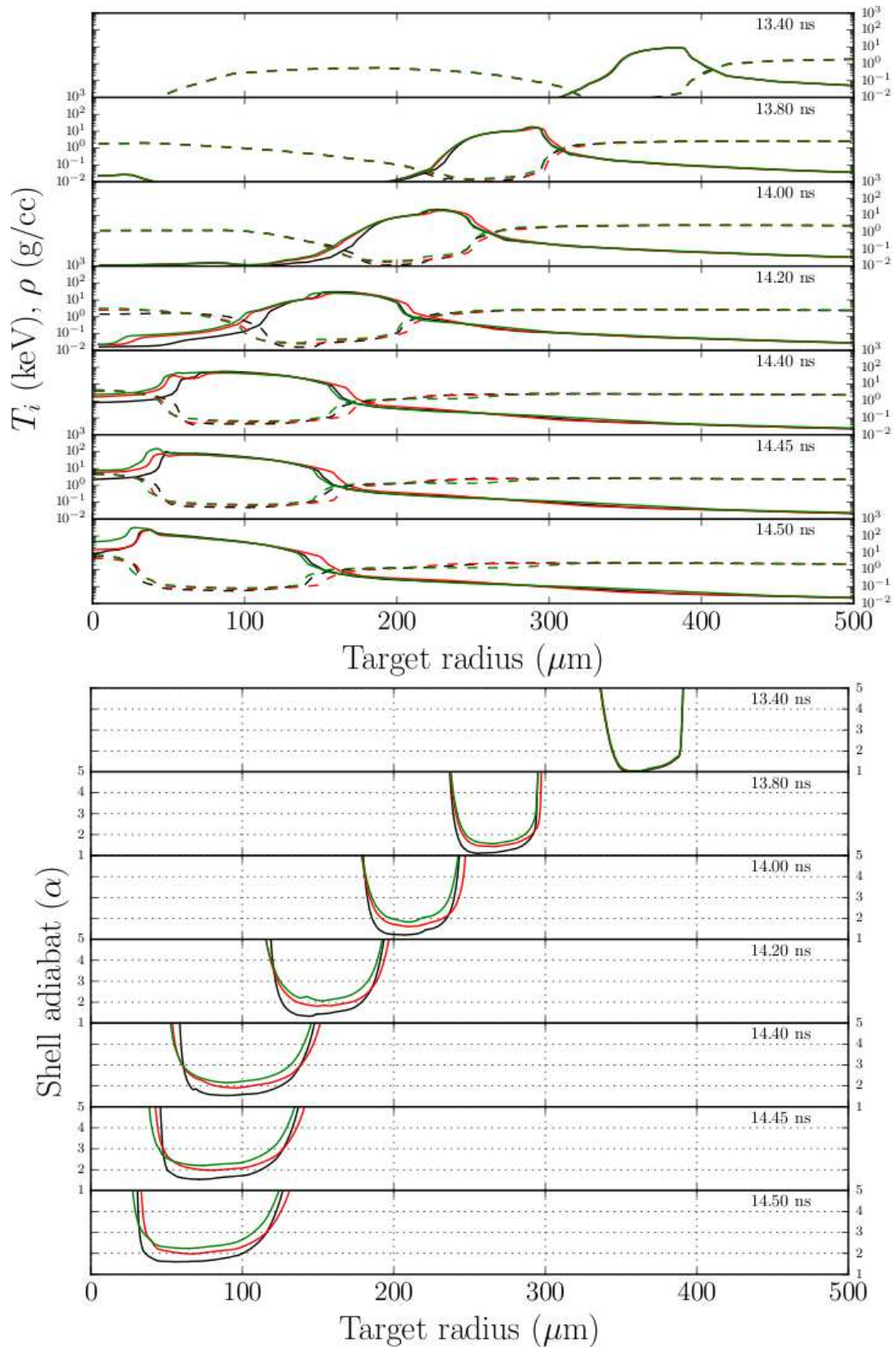
FIG. 13. (color) [top] Slices of plasma density ρ (in g/cc) indicated by plain lines, and ion temperature T_i (in keV) indicated by dashed lines, and [bottom] slices of the adiabat parameter α as a function of the target radii and for various times indicated on the upper-right corner of each subplot. Results from the simulation without HEs are shown in black and with HEs as colored lines; red for the $P_s = 200$ TW case and green for the $P_s = 300$ TW case
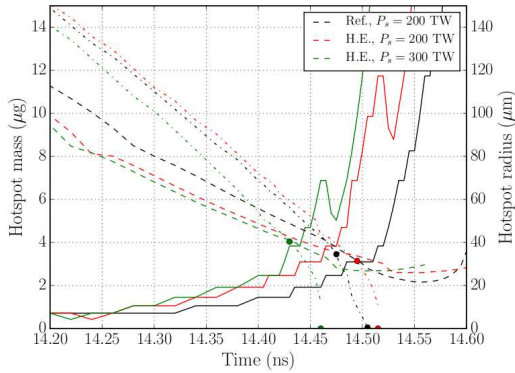
FIG. 14. (color) Mass of the hotspot as a function of time, indicated as plain lines. The hotspot radius is shown as dashed lines and the shock position as dotted dashed lines. The times when the shock enters into the hotspot and reaches the target center are indicated by colored circles. Data from the simulation without LPI-generated HEs is shown in black, and with the LPI-HE model with colored lines; red for the $P_s = 200$ TW case and green for the $P_s = 300$ TW case.

compared to the non-delayed case.

3. Hotspot properties

The thermodynamic path of the hotspot is shown in Fig. 16 for the reference case and the three cases with LPI-HEs at $t_s = 13.30$ ns. As expected from the analysis of the shell preheat, it is the case with the least hotspot density increase that obtains the highest yields. Indeed, the case with 200 TW spike power and $\Delta t_{HE} = 200$ ps reaches a marginal ignition, as can be seen from the vertical segment of the hotspot thermodynamic trajectory, that goes past the post temperature T_P. The yield in this case is of ~ 1 MJ only, as there is no transition from the deflagration to the detonation regime. This result highlights the potentially important role of the non-stationary phase of the HE generation on the target performance. Similarly, the 300 TW power case almost reaches ignition, as can be seen by the small loop in the thermodynamic path of the hotspot (the yield in that case is of ~ 0.1 MJ). This was expected given the results obtained in the pure-DT case: the inner-side shell ablation causing a rapid increase in the hotspot density and mass prior to the shock convergence can be compensated by a more powerful shock arriving earlier at the target center. However, the density increase still causes significant radiative losses, which are not compensated by a moderate α particle production here.

C. High power cases

The negative effect of the increase in hotspot mass prior to the ignitor shock arrival can be mitigated by a stronger ignitor shock. We investigate in this section the *high power cases* of $P_s \in [450, 500]$ TW for the CH-DT targets. Simulations with hot electrons at these spike powers were conducted for various shock launching times t_s. The target gains are reported in Fig. 11 [right]. Target ignition is reached with a maximum gain of 37 MJ for $P_s = 500$ TW and $t_s = 13.5$ ns, that is three quarters of the yield in the reference case without HEs. This can be attributed to a higher shell adiabat of $\alpha \sim 2.5$, compared to ~ 1.8 in the reference case. These spike powers correspond to peak ablation pressures of the order of 420 MBar. The thermodynamic paths of the hotspot for various launching times are given in Fig. 17.

Two main differences are observed with respect to the cases without hot electrons. First, the spike power required to reach ignition is about four times that of the case without hot electrons (~ 100 TW). In that target and laser configuration, the shock ignition scheme is arguably no longer a high gain approach: it requires a higher laser energy and power and produces a lower yield. The second difference is related to the width of the ignition window. The point design P_s, t_s with maximum gain lies on the right edge of the window. This can be determined by examining the relative timing of the ignitor shock entry in the hotspot with respect to the target stagnation time. Launching the ignitor shocks at later times t_s leads to a late shock entry in the hotspot with respect to the shell stagnation, which does not allow sufficient time for target burn (as can be seen for the $t_s = 13.6$ ns, $P_s = 500$ TW case). As a result, the ignition window, i.e. the time interval t_s in which target ignition occurs, is smaller by a factor of ~ 2 compared to the cases without hot electrons: about 150 ps compared to 300 ps in width. Specifically, the window is reduced on the left side of the maximum gain curve.

In the shock ignition scheme, the hotspot enters the ignition domain from the region of low temperatures where radiative losses dominate (see Fig. 17). The HEs increase the mass of the hostpot, therefore increasing the radiative losses and closing the ignition window in the time interval t_s where this HE-preheat is significant. This domain corresponds to the times at which the shell areal density is lower, namely for low values of the launching times t_s, i.e. on the left side of the maximum gain curve. This effect is illustrated in Fig. 18, by comparing the time-integrated radiative losses in the hotspot for various launching times t_s. In the case without hot electrons, the integrated radiative losses are the same prior to the ignitor shock arrival in the hotspot, whatever the value of t_s is, including for non-igniting targets. This is because the hotspot thermodynamic path is not affected by the shock launching time: the radiative loss curves in Fig. 18 [top] all follow the same path for different t_s and prior to the shock entry in the hotspot. Consequently, the shock timing values that lead to ignition are only determined by the shock entry time into the hotspot with respect to the stagnation dynamics (and by the spike power). On the contrary, in the case with hot electrons (see Fig. 18
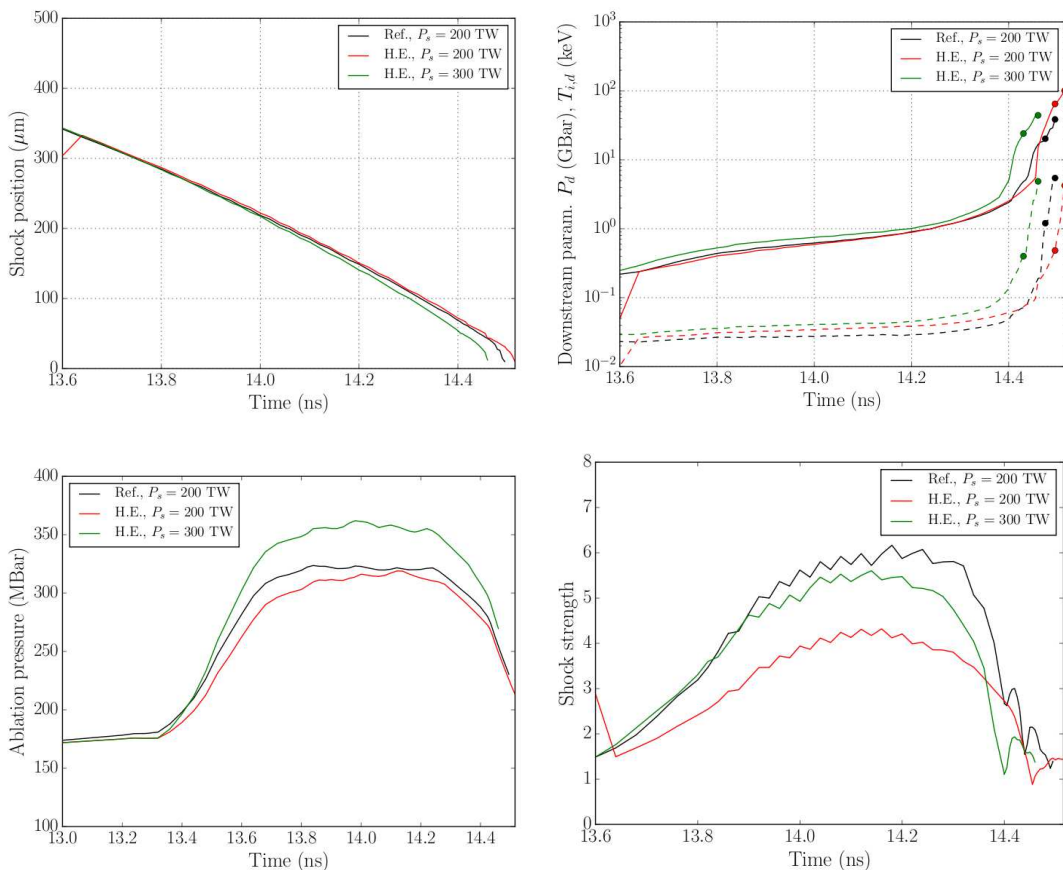
FIG. 15. (color) [top-left] Position of the strongest shock in the material. [top-right] Temperature (keV) and pressure (GBar) of the shocked plasma. The plain line indicates the downstream shock pressure and the dashed lines the downstream shock temperature. For each curve, the first circle represents the time when the shock enters into the hotspot, and the second circle indicates the time when the shock reaches the target center. [bottom-row] Time histories of [bottom-left] the ablation pressure and [bottom-right] the ignitor shock strength. For all panels, data from the simulation without LPI-generated HEs is shown in black, and with the LPI-HE model with colored lines; red for the $P_s = 200$ TW case and green for the $P_s = 300$ TW case. Note that $t = 13.6$ ns corresponds to the start of the ignitor spike plateau. Modulations on the bottom panels are due to automatic detection of the shock parameters.

[bottom]), these integrated radiative losses increase prior to the shock arrival. Consequently, the shock timing t_s not only determines the shock entry time with respect to the shell stagnation time, but also the initial radiative losses prior to shock entry in the hotspot. The latter are lower for later shock launching times due to the increased shell areal density, thus reducing the width of the ignition window on the left side of the maximum neutron curve.

VI. CONCLUSIONS

We have assessed the influence of LPI-generated HEs on the plasma dynamics of typical Shock Ignition ICF configurations, considering the pure-DT baseline HiPER target and a more elaborate CH-DT target. Hydrodynamic simulations of the ignition window were conducted with the PCGO model of laser propagation and absorp-

tion with or without LPI-HEs. In both target designs, the LPI-generated HEs are found to be detrimental to the target implosion. Although the shock downstream pressure is significantly increased with HEs, the latter have the adverse effect of causing an expansion of the inner surface of the imploding shell into the hotspot. The HE-induced inner ablation significantly increases the hotspot mass and density before the ignitor shock reaches the hotspot. Consequently: (i) the energy required to ignite the hotspot and (ii) the radiative losses are considerably increased. We have shown that the CH-DT target is more resilient to HEs, as the plastic ablator partially shields the imploding DT from the low energy part of the LPI-HE spectrum. However, by shielding the target to LPI-HEs, the amplification of the shock pressure due to the preheating decreases.

Additionally, it is found that the increased hotspot mass due to the preheat could be compensated by in-
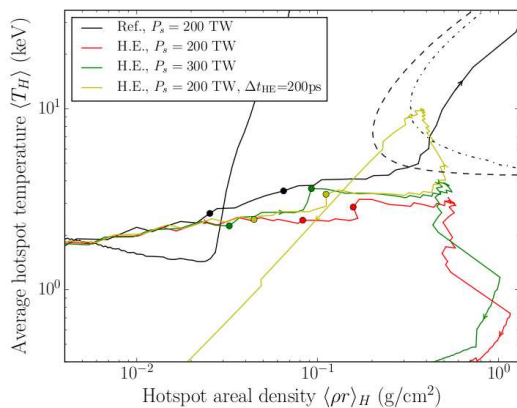
FIG. 16. (color) Thermodynamic path of the hotspot, for the case without LPI-generated HEs in black and with the LPI-HE model as colored lines; red for the $P_s = 200$ TW case, green for the $P_s = 300$ TW case and yellow for the case with $P_s = 200$ TW with HE generation delayed by 200 ps. The isobaric ignition curve is shown as a dashed line, and the non-isobaric curve with $\rho_{shell}/2 = \rho_h$ as a dotted dashed line[3]. Arrows indicate the direction of the time-dependent evolution of the hotspot. For each curve, the first dot indicates the time when the ignitor shock enters into the hotspot and the second indicates the time of shock rebounds on the target center.
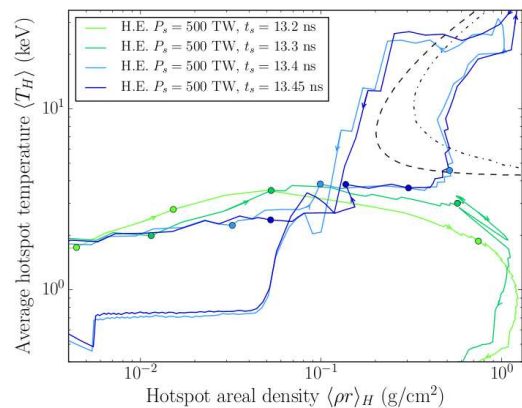

FIG. 17. (color) Thermodynamic path of the hotspot in the cases with LPI-HEs and $P_s = 500$ TW case for different values of $t_s \in [13.2; 13.45]$ ns. The isobaric ignition curve is shown as a dashed line, and the non-isobaric curve with $\rho_{shell}/2 = \rho_h$ as a dotted dashed line[3]. Arrows indicate the direction of the time-dependent evolution of the hotspot. For each curve, the first dot indicates the time when the ignitor shock enters into the hotspot, the second indicates the time of shock rebounds on the target center and the third indicates the time of shock collision with the shell.

creasing the spike power to at least 500 TW. Arguably, such high powers are incompatible with the high gain approach of shock ignition. Moreover, we have highlighted that the width of the ignition window at these high powers is greatly reduced on the left side of the maximum neutron curve, compared to the cases without LPI-generated HEs. This is a consequence of the increased radiative losses of the hotspot due to the mass increase prior to the shock arrival. Consequently, when considering LPI-generated HEs, the shock launching time no longer only determines the shock arrival time in the hotspot, but also the radiative preheat prior to the shock entry in the hotspot. These igniting targets produce three quarters of of the reference case gain, due to the increased shell adiabat. The preheat effect can be slightly mitigated by launching the HEs 200 ps after the start of the laser spike. However, this artificial delay is probably an overestimation of the transient phases of SRS and TPD, given the large scale lengths at play here.

This Shock Ignition study indicates that the effects of the LPI-generated HEs on the target dynamic are significant and cannot be ignored. Considering conventional designs, the HEs may also be responsible for failures of target ignitions. As such, it appears necessary to include the effects of LPI-generated HEs in any realistic target design and physical related tools. Here we have highlighted the importance of the hotspot mass increase caused by the shell preheat and the interplay between shock pressure and target preheat. However, the LPI-HEs may also play a role in the collision of the return shock with the ignitor shock, which was not studied here.

Finally, it is interesting to consider the potential effect of CBET on the LPI-HEs. In a direct-drive configuration, CBET redistributes the laser intensity away from the critical density[38]. This redistribution arises from the geometry of the interacting beams and takes place from the sonic point up to the Mach=5 point. Consequently, depending on the beam configuration, CBET may or may not deplete the incident beam energy before the quarter critical density where most of the HE flux is generated. Finally, we note that the decreased convergence caused by CBET implies that higher laser intensities may be necessary, thus increasing the LPI-HE flux.

VII. ACKNOWLEDGMENTS

[1] V. Shcherbakov, Sov. J. Plasma Phys. (Engl. Transl.); (United States) **9:2** (1983).

[2] R. Betti, C. D. Zhou, K. S. Anderson, L. J. Perkins, W. Theobald, and A. A. Solodov, Physical Review Letters **98**, 155001 (2007).

[3] X. Ribeyre, M. Lafon, G. Schurtz, M. Olazabal-Loumé, J. Breil, S. Galera, and S. Weber, Plasma Physics and Controlled Fusion **51**, 124030 (2009).
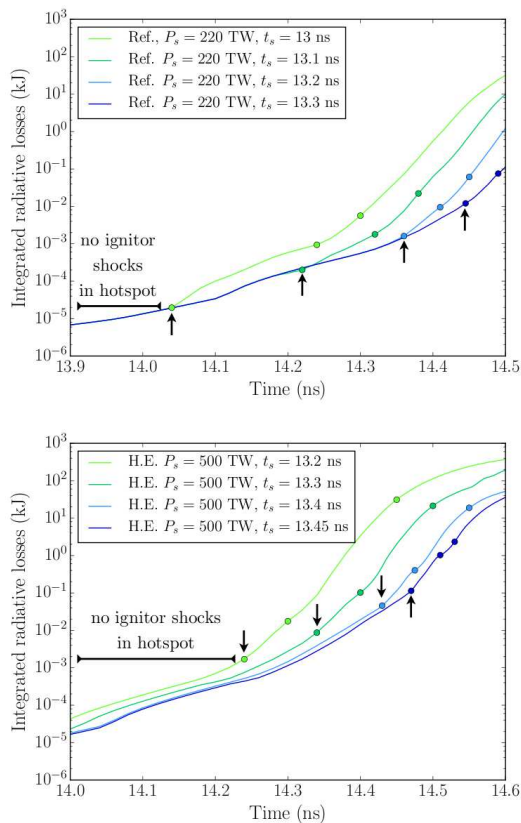
FIG. 18. (color) Integrated radiative losses $E_B(t) = \int_0^t \mathcal{W}_B(t)\mathrm{d}t$ as a function of time, in kJ. [Top] simulation results for $P_s = 220$ TW and without LPI-HEs, at various values of t_s, and [bottom] simulation results for $P_s = 500$ TW with LPI-HEs, at various values of t_s. In each panel, the two earliest timings correspond to simulations that do not predict the target ignition. The dots indicate the time when the ignitor shock enters into the hotspot, the time of shock rebounds on the target center and the time of shock collision with the shell. Arrows underline the time of shock entry in the hotspot for each case.

[4] L. J. Perkins, R. Betti, K. N. Lafortune, and W. H. Williams, Physical Review Letters **103**, 045004 (2009).

[5] D. Batani, L. Antonelli, S. Atzeni, L. Antonelli, S. Atzeni, J. Badziak, F. Baffigi, T. Chodukowski, F. Consoli, G. Cristoforetti, R. D. Angelis, R. Dudzak, G. Folpini, L. Giuffrida, L. A. Gizzi, Z. Kalinowska, P. Koester, E. Krousky, M. Krus, L. Labate, T. Levato, Y. Maheut, G. Malka, D. Margarone, A. Marocchino, J. Nejdl, P. Nicolai, T. O'Dell, T. Pisarczyk, O. Renner, Y. J. Rhee, X. Ribeyre, M. Richetta, M. Rosinski, M. Sawicka, A. Schiavi, J. Skala, M. Smid, C. Spindloe, J. Ullschmied, A. Velyhan, and T. Vinci, Physics of Plasmas **21**, 032710 (2014).

[6] M. Hohenberger, W. Theobald, S. X. Hu, K. S. Anderson, R. Betti, T. R. Boehly, A. Casner, D. E. Fratanduono, M. Lafon, D. D. Meyerhofer, R. Nora, X. Ribeyre, T. C. Sangster, G. Schurtz, W. Seka, C. Stoeckl, and B. Yaakobi, Physics of Plasmas **21**, 022702 (2014).

[7] A. Colaïtis, G. Duchateau, X. Ribeyre, Y. Maheut, G. Boutoux, L. Antonelli, P. Nicolaï, D. Batani, and V. Tikhonchuk, Phys. Rev. E **92**, 041101 (2015).

[8] R. Nora, W. Theobald, R. Betti, F. Marshall, D. Michel, W. Seka, B. Yaakobi, M. Lafon, C. Stoeckl, J. Delettrez, A. Solodov, A. Casner, C. Reverdin, X. Ribeyre, A. Vallet, J. Peebles, F. Beg, and M. Wei, Phys. Rev. Lett. **114**, 045001 (2015).

[9] W. Theobald, R. Nora, W. Seka, M. Lafon, K. S. Anderson, M. Hohenberger, F. J. Marshall, D. T. Michel, A. A. Solodov, C. Stoeckl, D. H. Edgell, B. Yaakobi, A. Casner, C. Reverdin, X. Ribeyre, A. Shvydky, A. Vallet, J. Peebles, F. N. Beg, M. S. Wei, and R. Betti, Physics of Plasmas **22**, 056310 (2015).

[10] X. Ribeyre, V. T. Tikhonchuk, J. Breil, M. Lafon, and E. Le Bel, Physics of Plasmas **18**, 102702 (2011).

[11] A. Vallet, X. Ribeyre, and V. Tikhonchuk, Physics of Plasmas **20**, 082702 (2013).

[12] A. Vallet, *Hydrodynamic modeling of the shock ignition scheme for inertial confinement fusion (in French)*, Ph.D. thesis, Université Bordeaux (2014).

[13] L. Antonelli, M. Richetta, P. Koester, L. Labate, T. Levato, L. Gizzi, E. Krousky, J. Skala, R. Dubzak, J. Ullshimied, O. Renner, M. Smid, M. Rosinski, J. Badziak, T. Pisarczyk, Z. Kalinowska, and T. Chodukowski, in *Proceedings of 39th EPS Conference & 16th Int. Congress on Plasma Physics* (2013).

[14] P. Koester, L. Antonelli, S. Atzeni, J. Badziak, F. Baffigi, D. Batani, C. A. Cecchetti, T. Chodukowski, F. Consoli, G. Cristoforetti, R. D. Angelis, G. Folpini, L. A. Gizzi, Z. Kalinowska, E. Krousky, M. Kucharik, L. Labate, T. Levato, R. Liska, G. Malka, Y. Maheut, A. Marocchino, P. Nicolai, T. O'Dell, P. Parys, T. Pisarczyk, P. Raczka, O. Renner, Y. J. Rhee, X. Ribeyre, M. Richetta, M. Rosinski, L. Ryc, J. Skala, A. Schiavi, G. Schurtz, M. Smid, C. Spindloe, J. Ullschmied, J. Wolowski, and A. Zaras, Plasma Physics and Controlled Fusion **55**, 124045 (2013).

[15] O. Klimo and V. T. Tikhonchuk, Plasma Physics and Controlled Fusion **55**, 095002 (2013).

[16] D. Batani, S. Baton, A. Casner, S. Depierreux, M. Hohenberger, O. Klimo, M. Koenig, C. Labaune, X. Ribeyre, C. Rousseaux, G. Schurtz, W. Theobald, and V. Tikhonchuk, Nuclear Fusion **54**, 054009 (2014).

[17] J. F. Myatt, J. Zhang, J. A. Delettrez, A. V. Maximov, R. W. Short, W. Seka, D. H. Edgell, D. F. DuBois, D. A. Russell, and H. X. Vu, Physics of Plasmas **19**, 022707 (2012).

[18] H. X. Vu, D. F. DuBois, J. F. Myatt, and D. A. Russell, Physics of Plasmas **19**, 102703 (2012).

[19] S. Gus'kov, X. Ribeyre, M. Touati, J.-L. Feugeas, P. Nicolaï, and V. Tikhonchuk, Physical Review Letters **109**, 255004 (2012).

[20] K. Jungwirth, A. Cejnarova, L. Juha, B. Kralikova, J. Krasa, E. Krousky, P. Krupickova, L. Laska, K. Masek, T. Mocek, M. Pfeifer, A. Präg, O. Renner, K. Rohlena, B. Rus, J. Skala, P. Straka, and J. Ullschmied, Physics of Plasmas **8**, 2495 (2001).

[21] T. Boehly, D. Brown, R. Craxton, R. Keck, J. Knauer, J. Kelly, T. Kessler, S. Kumpan, S. Loucks, S. Letzring, F. Marshall, R. McCrory, S. Morse, W. Seka, J. Soures, and C. Verdon, Optics Communications **133**, 495 (1997).

[22] P. Nicolaï, J.-L. Feugeas, M. Touati, X. Ribeyre, S. Gus'kov, and V. Tikhonchuk, Phys. Rev. E **89**, 033107 (2014).

[23] V. T. Tikhonchuk, A. C. is, A. Vallet, E. L. Aisa, G. Duchateau, P. Nicolaï, and X. Ribeyre, Plasma Physics and Controlled Fusion **58**, 014018 (2016).

[24] J. Breil, S. Galera, and P. H. Maire, Computers & Fluids **46**, 161 (2011).

[25] S. Atzeni, A. Marocchino, A. Schiavi, and G. Schurtz, New Journal of Physics **15**, 045004 (2013).

[26] T. B. Kaiser, Phys. Rev. E **61**, 895 (2000).

[27] A. Colaïtis, G. Duchateau, P. Nicolaï, and V. Tikhonchuk, Phys. Rev. E **89**, 033101 (2014).

[28] Y. A. Kravtsov and N. Y. Zhu, *Theory of Diffraction, Heuristic Approaches*, Alpha Science Series on Wave Phenomena (Alpha Science International LTD., Oxford, U.K., 2010).

[29] A. Colaïtis, *Multiscale description of the laser-plasma interaction: application to the physics of shock ignition in inertial confinement fusion (in English)*, Ph.D. thesis, Université de Bor-

deaux (2015).

[30] C. K. Li and R. D. Petrasso, Phys. Rev. E **70**, 067401 (2004).

[31] S. P. Regan, R. Epstein, V. N. Goncharov, I. V. Igumenshchev, D. Li, P. B. Radha, H. Sawada, W. Seka, T. R. Boehly, J. A. Delettrez, O. V. Gotchev, J. P. Knauer, J. A. Marozas, F. J. Marshall, R. L. McCrory, P. W. McKenty, D. D. Meyerhofer, T. C. Sangster, D. Shvarts, S. Skupsky, V. A. Smalyuk, B. Yaakobi, and R. C. Mancini, Physics of Plasmas **14**, 056305 (2007).

[32] S. Atzeni, A. Schiavi, and C. Bellei, Physics of Plasmas **14**, 052702 (2007).

[33] A. J. Schmitt, J. W. Bates, S. P. Obenschain, S. T. Zalesak, and D. E. Fyfe, Physics of Plasmas **17**, 042701 (2010).

[34] B. Canaud, S. Laffite, and M. Temporal, Nuclear Fusion **51**, 062001 (2011).

[35] K. S. Anderson, R. Betti, P. W. McKenty, T. J. B. Collins, M. Hohenberger, W. Theobald, R. S. Craxton, J. A. Delettrez, M. Lafon, J. A. Marozas, R. Nora, S. Skupsky, and A. Shvydky, Physics of Plasmas **20**, 056312 (2013),

http://dx.doi.org/10.1063/1.4804635.

[36] V. Brandon, B. Canaud, M. Temporal, and R. Ramis, Nuclear Fusion **54**, 083016 (2014).

[37] J. Garnier, C. Gouédard, and L. Videau, Optics Communications **176**, 281 (2000).

[38] A. Colaïtis, G. Duchateau, X. Ribeyre, and V. Tikhonchuk, Phys. Rev. E **91**, 013102 (2015).

[39] X. Ribeyre, S. Gus'kov, J.-L. Feugeas, P. Nicolaï, and V. T. Tikhonchuk, Physics of Plasmas **20**, 062705 (2013).

[40] S. Atzeni and J. Meyer-ter Vehn, *The Physics of Inertial Fusion*, International Series of Monographs on Physics (Oxford University Press, Oxford, 2004).

[41] Medium power with respect to the *high power* cases at 450 and 500 TW presented in Sec. V C.

[42] This upper limit imposed in the model for the TPD-HE average temperature follows from experimental observations[7,8,29].